Phage-guided modulation of the gut microbiota of mouse models of colorectal cancer augments their responses to chemotherapy

Di-Wei Zheng[1,2], Xue Dong[1,2], Pei Pan[1], Ke-Wei Chen[1], Jin-Xuan Fan[1], Si-Xue Cheng[1] and Xian-Zheng Zhang [ID][1]*

The microbiota in the human gut is strongly correlated with the progression of colorectal cancer (CRC) and with therapeutic responses to CRC. Here, by leveraging the higher concentration of the pro-tumoural *Fusobacterium nucleatum* and the absence of antineoplastic butyrate-producing bacteria in the faecal microbiota of patients with CRC, we show that—in mice with ortho-topic colorectal tumours or with spontaneously formed colorectal tumours—oral or intravenous administration of irinotecan-loaded dextran nanoparticles covalently linked to azide-modified phages that inhibit the growth of *F. nucleatum* significantly augments the efficiency of first-line chemotherapy treatments of CRC. We also show that oral administration of the phage-guided irinotecan-loaded nanoparticles in piglets led to negligible changes in haemocyte counts, immunoglobulin and hista-mine levels, and liver and renal functions. Phage-guided nanotechnology for the modulation of the gut microbiota might inspire new approaches for the treatment of CRC.

The gut microbiota comprises approximately 100 trillion (10^{14}) bacterial cells[1]. These bacteria perform critical functions in the physiology of the host, and can even be considered to be a microbial organ[2] that not only plays an important role in acute infection, chronic-disease occurrence and tumour progression, but also offers new areas of study for the development of new therapies[3]. Transplants of faecal microbiota are considered to be a standard-of-care therapy for recurrent patients with severe infections with *Clostridium difficile*[4]. For diseases such as Crohn's disease, autoim-munity and atherosclerosis, antibiotics that inhibit harmful micro-organisms have shown superior therapeutic effects[5–7].

Recent studies suggest that the microbiota contributes to both the pathogenesis and prognosis of CRCs[8–12], yet the complex interplay between gut microbiota and CRC is a major obstacle for the devel-opment of faecal microbiota transplants and therapy using antibi-otics to treat CRC. In fact, the gut microbiota can both promote and inhibit CRC[13]. Among the microorganisms, *Fusobacterium* is well known to drive the formation of a pro-tumoural microenvi-ronment that is highly chemoresistant and immunosuppressive[14,15]. Clinically, the abnormal proliferation of *Fusobacterium* was found to directly induce the failure of chemotherapy[16]. By contrast, short-chain fatty acids (SCFAs) produced by fermentative bacteria are known to suppress the growth of CRC and induce anticancer immune responses[17,18]. Owing to the diverse roles of the gut micro-biota, antibiotics used for the elimination of bacteria shows only limited therapeutic effects in CRC[19]. This is because antibiotics non-selectively kill both pro-tumoural and antineoplastic bacteria[20]. A strategy capable of controllably leveraging the gut microbiota in the treatment of CRC is therefore highly desirable.

Here we describe a gut-microbiota modulatory therapy based on phage-guided biotic–abiotic hybrid nanomaterials (Fig. 1a). As most phages are specific to certain bacteria, the phage therapy should be particularly suitable for accurately removing pro-tumoural

bacteria[21–23]. We isolated a phage strain from human saliva that could specifically lyse *F. nucleatum*. Prebiotics such as dextran and oligosaccharides are known to have a function in shaping the gut microbiota and in promoting the production of SCFAs[24]. We encap-sulated irinotecan (IRT)—a first-line drug against CRC—within dextran nanoparticles (DNPs) to form IRT-loaded DNPs (IDNPs). Using a bioorthogonal reaction[25], we covalently linked azodibenzo-cyclooctyne (DBCO)-modified IDNPs (D-IDNPs) to azide-modi-fied phages (A-phages) to construct a phage-guided biotic–abiotic hybrid nanosystem. We show that A-phages accumulated in CRC tumours in vivo, and that the oral administration of the biotic–abi-otic hybrid nanosystem eliminated intratumoural *F. nucleatum*. This bioorthogonal strategy improves the accumulation of the nanocarri-ers in the tumours, thereby reducing the side effects of chemother-apy drugs, which can also accumulate in normal tissues. DNPs could also promote the proliferation of endogenic *Clostridium butyricum* and enhance the levels of colonic SCFA. A series of experiments were designed and carried out in mice, piglets and in clinical patient samples to demonstrate the effectiveness and biosafety of our gut-microbiota regulation strategy. Our approach might inspire future treatment strategies for colon tumours colonized with *F. nucleatum*.

Screening for CRC-associated bacteria

To investigate the role of gut microbiota in the development of CRC and its potential capacity for modulating cancer treatment, we analysed metagenomic sequence data[26]—extracted from the NCBI Sequencing Read Archive (SRA) database (PRJEB10878)—from fae-cal samples of 72 patients with CRC and 52 controls. Identified reads of pro-tumoural and anti-tumoural bacteria in the 16S ribosomal DNA (16S rDNA) data that were extracted from these faecal sam-ples are presented in Fig. 1b. Significant enrichment of *F. nucleatum* was found in the faecal samples obtained from patients with CRC. A decrease in butyrate-producing Firmicutes (mainly *Roseburia*

[1]Key Laboratory of Biomedical Polymers of Ministry of Education & Department of Chemistry, Wuhan University, Wuhan, China. [2]These authors contributed equally: Di-Wei Zheng, Xue Dong. *e-mail: xz-zhang@whu.edu.cn
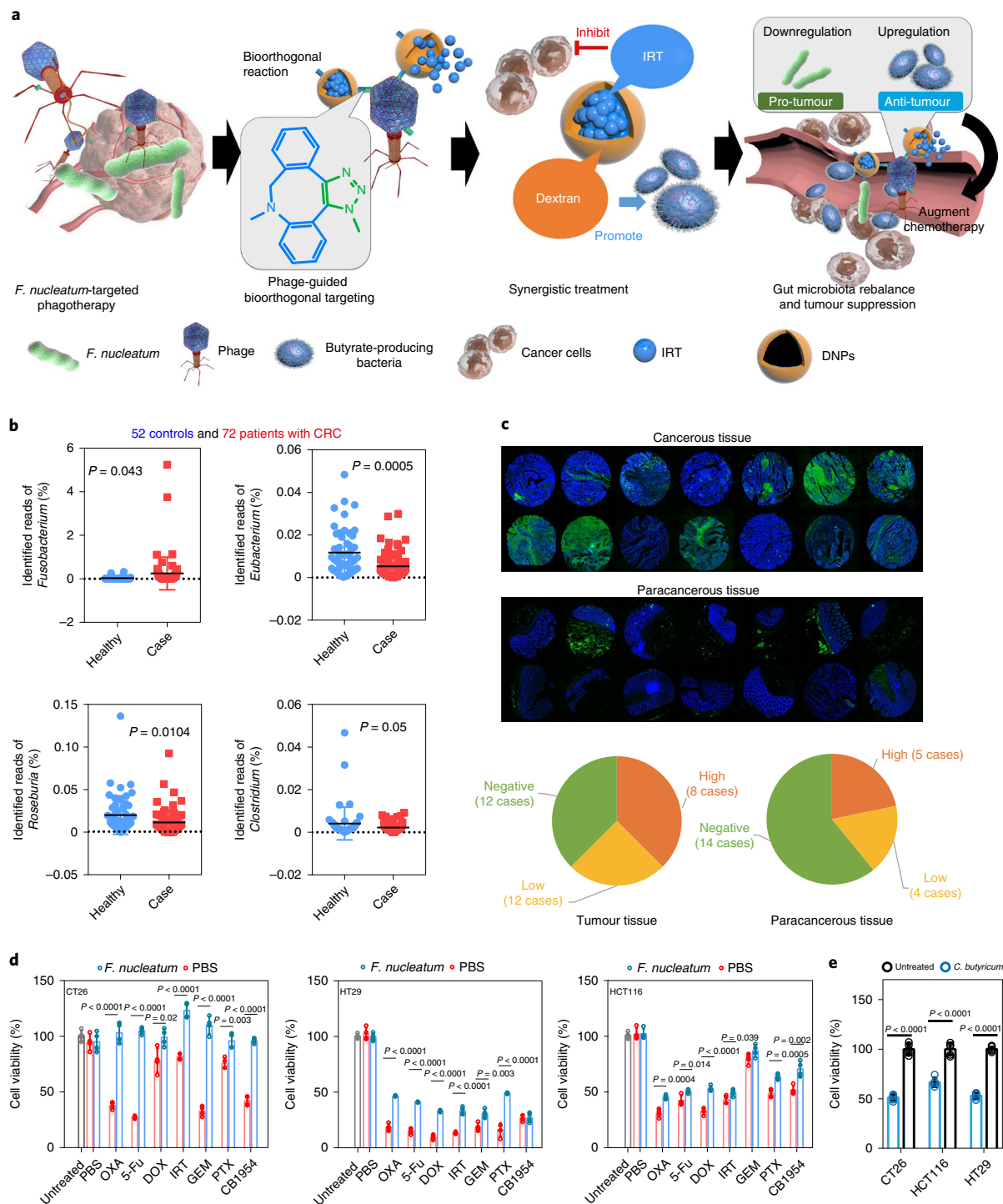
Fig. 1 | Screening for phages with pro-tumoural and anti-tumoural effects in CRC. a, Illustration of the phage-guided biotic–abiotic hybrid nanosystem and its therapeutic effects. A strain of phage was isolated for targeting CRC and eliminating the pro-tumoural *Fusobacterium*. IDNPs then bind to phages pre-accumulated in CRC tumours using a bioorthogonal chemistry strategy. DNPs enhance the production of anti-tumoural bacterial butyrate. The inhibition of pro-tumoural bacteria and the promotion of anti-tumoural bacteria together augment the efficacy of chemotherapy and reduce its side effects. **b**, Levels of *Fusobacterium*, *Eubacterium*, *Roseburia* and *Clostridium* in faecal samples obtained from patients with CRC ($n=72$) and healthy people ($n=52$) from NCBI Bioproject (PRJEB10878). The identified reads of each bacteria and total sequenced 16S rDNA were compared. **c**, Representative images of FISH assays measuring the level of *F. nucleatum* in tumour tissue ($n=32$) and paracancerous tissue ($n=23$) samples obtained from patients with CRC. Green fluorescence represents *F. nucleatum*. The number of positive fluorescent dots was counted. The ratio of *F. nucleatum* fluorescent dots:nuclei number was measured for data analysis (high, ratio >0.05; low, ratio >0.01; negative, ratio <0.01). **d**, The effect of *F. nucleatum* in rescuing CRC cells (CT26 (left), HT29 (middle) and HCT116 (right)) from cell death induced by oxaliplatin (OXA), 5-fluorouracil (5-Fu), doxorubicin (DOX), IRT, gemcitabine (GEM), paclitaxel (PTX) and CB1954. Four biological replicates are shown. Experiments were repeated three times. **e**, The anticancer effect of *C. butyricum* in CRC cells (CT26, HT29 and HCT116). Five biological replicates are shown. Experiments were repeated three times. Significance between groups was calculated using an unpaired two-tailed Student's *t*-test (**b**, **d** and **e**). Data are mean ± s.d.

intestinalis, *C. butyricum* and *Eubacterium rectale*) was also observed in response to the occurrence of CRC. We analysed both tumour and paracancerous tissue samples obtained from patients with CRC. We used fluorescence in situ hybridization (FISH) to stain *F. nucleatum* in these clinical samples (Supplementary Fig. 1a,b). We found that the majority of *F. nucleatum* colonizes specifically in the cancer tissues or adheres to the mucosa (Fig. 1c). We also observed a limited number of bacteria in paracarcinoma tissues. The semiquantitative analysis also led us to the same conclusion, with *F. nucleatum* being detected in 62.5% (20 out of 32) of CRC tissues; by contrast, only 9 cases of *F. nucleatum*-positive samples were observed in paracarcinoma tissues.

We then analysed gut microbiota in mouse models, including colitis-associated cancer (azoxymethane- and dextran sulfate sodium-treated mice) and spontaneous colonic neoplasms (C57BL/6J *Apc*[Min/+] mice). By using 16S rDNA identification, we observed that the gut microbiota in *Apc*[Min/+] mice had a change consistent with the clinical outcome in human patients with CRC; increased levels of *F. nucleatum* and decreased levels of butyrate-producing bacteria were found. We observed a loss of species richness (Supplementary Fig. 2a); the decline in the diversity of microbial species is a universal phenomenon in patients[27].

Subsequently, we investigated the biological effects of *F. nucleatum* and *C. butyricum* in CRC cell lines. When chemotherapeutic agents were added, *F. nucleatum* was found to enhance the chemoresistance of CRC cell lines. The cytotoxicity of almost all of the drugs was completely inhibited in mouse CT26 and human HT29 cells (Fig. 1d). In HCT116 cells, only the effect of gemcitabine was not affected by the presence of bacteria. Considering the poor clinical prognosis of patients who are positive for *F. nucleatum*, eliminating the tumour-infiltrating bacteria and reversing the multidrug resistance of CRC would be necessary. Furthermore, we noticed that butyrate-producing bacteria (such as *C. butyricum*) could markedly suppress the growth of CRC cells (Fig. 1e).

Effective elimination of *F. nucleatum* by phages

We analysed faecal samples from male C57BL/6J *Apc*[Min/+] mice and saliva samples obtained from healthy volunteers. In a double-layered brain–heart infusion (BHI) broth, two types of phages isolated from mouse faeces (P1) and human saliva (P2) showed the capacity to inhibit the growth of *F. nucleatum*. These phages were purified for further study. The antibacterial effects of P1 and P2 were tested in five different bacteria (Fig. 2a,b), including *F. nucleatum* (ATCC

10953), *Bacillus subtilis* (ATCC 6051), *Bacillus thuringiensis* (ATCC 10792), *Escherichia coli* (strain MG1655) and *C. butyricum* (ATCC 19398). P1 phages showed a broad antibacterial spectrum. By contrast, P2 phages selectively suppressed the proliferation of *F. nucleatum*, whereas other bacteria were completely unaffected. The same result was confirmed by the fluorescence labelling method. Red fluorescent rhodamine-B (RhB)-labelled P2 phages were shown to be well adhered to the green fluorescent fluorescein isothiocyanate (FITC)-labelled *F. nucleatum*[28] (Fig. 2c). Other *F. nucleatum* strains were then tested for susceptibility to P2 phages. As shown in Fig. 2d, P2 phages could suppress the growth of these *F. nucleatum* strains; however, the inhibition efficiency of P2 differed between different strains, suggesting that different subspecies might express different levels of phage receptors.

The phage genetic material was isolated and treated with deoxyribonuclease (DNase), ribonuclease (RNase) and various restriction enzymes. DNase and some restriction enzymes were able to cut the genome (Fig. 2e). The size of the P2 genome was estimated by calculating the sum of the size of each DNA fragment after digestion with HindIII (Supplementary Fig. 3a). On the basis of these results, we deduced that the genetic material of P2 phages should be a double-stranded DNA (~4.5 kb). KpnI was found to digest the DNA into a large fragment and a small fragment (~2 kb). P2 phages might be temperate phages that could reproduce using both the lytic and the lysogenic cycles (Supplementary Fig. 3b–c). After confirming the biological properties, P2 phages were chosen for further studies.

After co-incubation with *F. nucleatum*, resistance to chemotherapy could be effectively reversed in both mouse cells (CT26) and human cells (HCT116 and HT29) after treatment with the P2 phage (Fig. 2f). The efficacy of phages in living animals was evaluated. Phages were intragastrically administered or intravenously injected into *Apc*[Min/+] mice. As shown in Fig. 2g, by comparing the alterations induced by these two administration schemes, we noticed that both methods could substantially eliminate the gut *Fusobacterium*. By contrast, it was found that the antibiotic treatment killed those bacteria uniformly. The specific targeting capacity of phages was then tested in clinical CRC samples. *F. nucleatum* in multiple tissue sections was stained with a FISH probe (green fluorescence). The red-fluorescent-labelled phages mostly overlapped with the staining of *F. nucleatum* (Fig. 2h). This result confirmed that this phage-mediated therapy might be achieved in the complex intestinal environment.

We then carried out transcriptomics in CT26 cells to elucidate the mechanism by which *F. nucleatum* induces resistance to

Fig. 2 | Phages eliminating *F. nucleatum*-induced chemotherapy resistance in vitro. a,b, In vitro lysis of different species of bacteria by P1 (**a**) and P2 (**b**) phages. Six biological replicates were measured. Experiments were repeated three times. **c,** In vitro phage-binding assays of P2 phages binding to different species of bacteria. Phages were marked with red fluorescent RhB and bacteria were labelled with FITC. Experiments were repeated two times and images from one experiment out of a total of two experiments are shown. Four images were captured per group. Scale bars, 5 μm. **d,** In vitro lysis of different strains of *F. nucleatum* by P2 phages. Four biological replicates are shown. Experiments were repeated three times. **e,** Restriction enzyme digestion of P2 nucleic acids (stained with GelRed) electrophoresed on an agarose gel. Genomic nucleic acids of P2 phages were digested with DNase, RNase or various restriction enzymes. **f,** In vitro anticancer effect of both phage and chemotherapy (IDNP) in a CRC cell–*F. nucleatum* (*Fn*) co-culture system. Six biological replicates are shown. M, marker. **g,** Changes in the levels of *F. nucleatum* and *C. butyricum* (*Cb*) in faecal samples collected from *Apc*[Min/+] mice after receiving intragastric (i.g.) or intravenous (i.v.) administration of phages (*F. nucleatum*-specific P2 phages or *E. coli*-specific M13 phages) and antibiotics. Five biological replicates are shown. Experiments were repeated three times. **h,** Ex vivo phage-binding assays of P2 phages in the microchip of tumour tissues and paracancerous pairs from patients with CRC (phages and *F. nucleatum* were labelled with cyanine 5 (Cy5) and FITC, respectively). Arrow heads indicate the overlap between *F. nucleatum* and phage. DAPI, 4,6-diamidino-2-phenylindole. Scale bar, 50 μm. **i,** Differential gene expression heat map of identified genes involved in the pathway of autophagy. Three biological replicates were measured. A transcriptomics study indicated that the use of phages could inhibit the protective autophagy meditated by *F. nucleatum*. Pathway analysis was performed using gene ontology pathway analysis. **j,** TEM images of CT26 cells after 4 h of different treatments. Five images were captured per group. Scale bars, 2 μm. **k,** The effect of various inhibitors (3-MA, an inhibitor of autophagy; Fer-1, an inhibitor of ferroptosis; Nec-1, an inhibitor of necroptosis; and Ac-DEVD-CHO, an inhibitor of apoptosis) on CT26 cells treated with chemotherapy, chemotherapy and *F. nucleatum* or chemotherapy, *F. nucleatum* and phages. Six biological replicates are shown. Experiments were repeated two times. **l,** A possible mechanism by which *F. nucleatum* induces protective autophagy against apoptosis. Significance between groups of two was calculated using two-tailed Student's *t*-tests (**d**), one-way analysis of variance (ANOVA; **a** and **b**) or one-way ANOVA with Tukey's post hoc test (**f**, **g** and **k**). Data are mean ± s.d.

chemotherapy in CRC. A total of 12,840 genes were analysed, and an absolute fold change > 1.5 with a P value < 0.05 was set as a threshold to define the differentially expressed genes (Supplementary

Fig. 4a–d). Differentially expressed genes in groups that were co-incubated with *F. nucleatum* and treated with phages were studied further. On the basis of gene ontology enrichment analysis, we
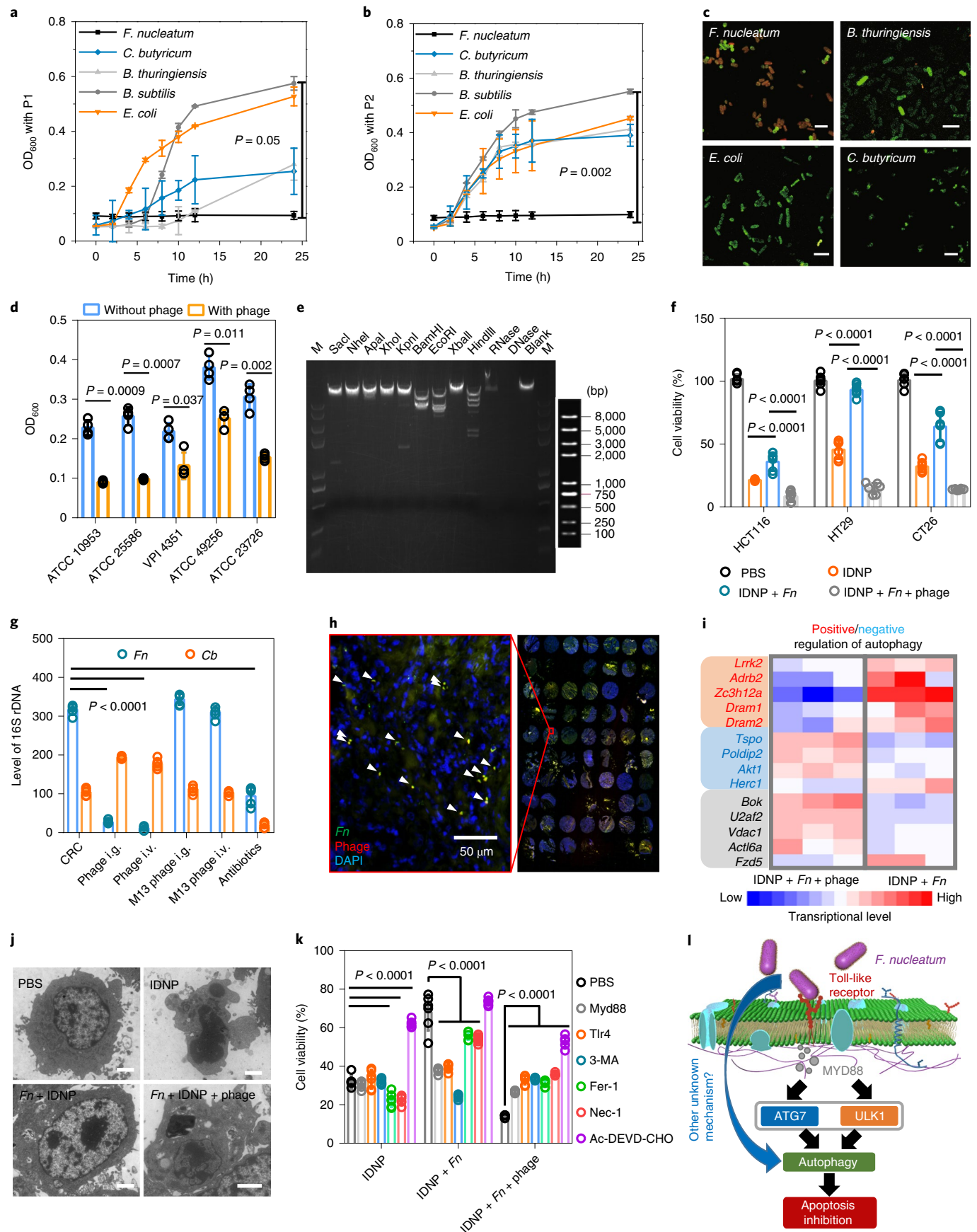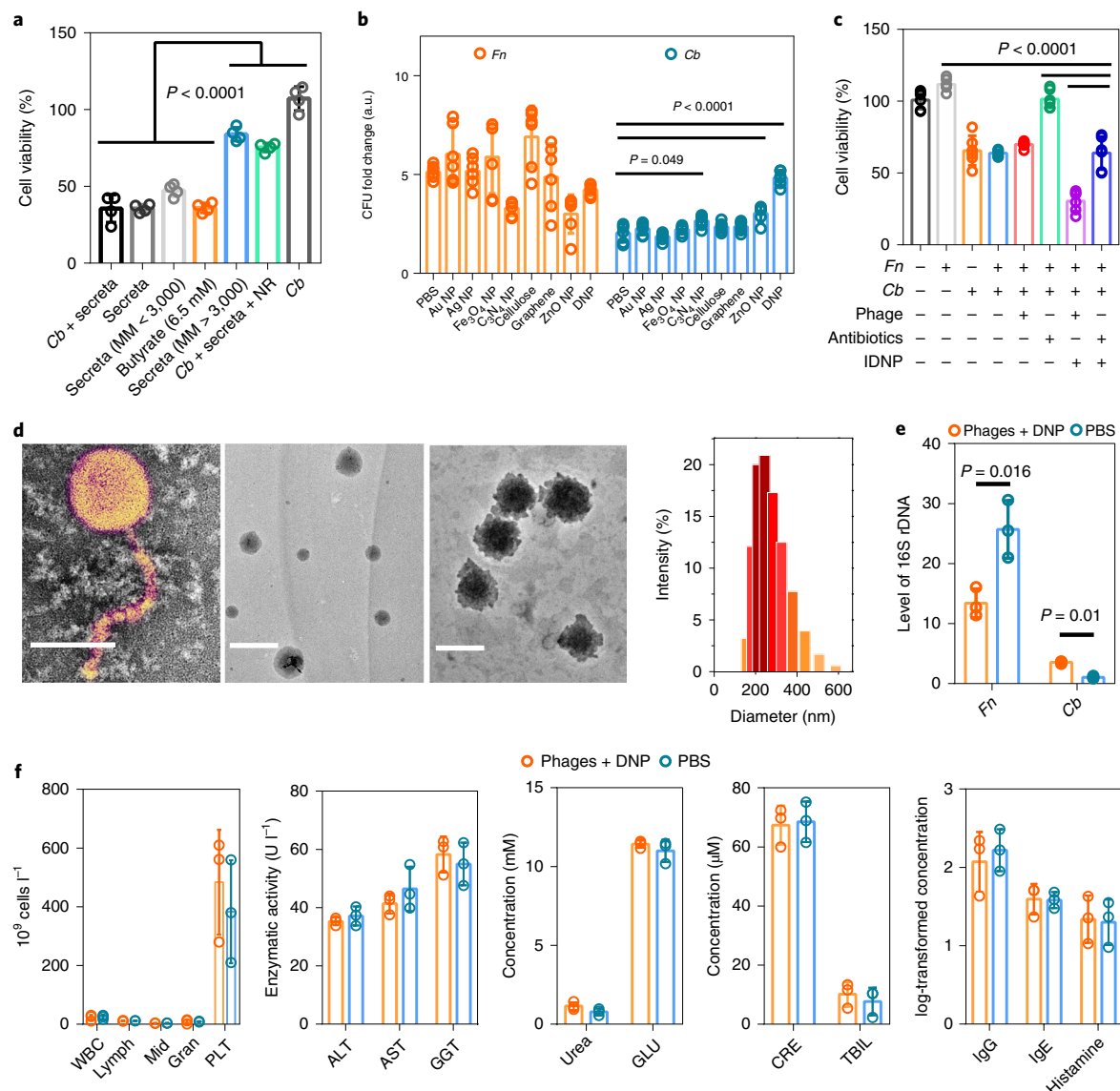
Fig. 3 | In vitro anticancer effect of IDNPs. a, To study of the mechanism that underlies the anticancer effect of *C. butyricum*, CT26 cells were treated with a diverse range of agents, including *C. butyricum* (10⁷ colony forming units (CFU) ml⁻¹) with BHI medium containing *C. butyricum* secreta (*Cb* + secreta), BHI medium containing *C. butyricum* secreta (secreta), BHI medium containing small molecules with a molecular mass < 3,000 Da (secreta (MM < 3,000)), butyrate solution (6.5 mM), BHI medium containing macromolecules with a molecular mass > 3,000 Da (secreta (MM > 3,000)), *C. butyricum* with BHI medium containing *C. butyricum* secreta and NR (*Cb* + secreta + NR), and *C. butyricum* without BHI medium (*Cb*). Four biological replicates are shown. **b**, A screen of the effect of eight different types of nanoparticles (NP; 0.5 mg ml⁻¹) on the proliferation of *F. nucleatum* and *C. butyricum*. CFU fold change represents the ratio of the density of bacteria after the treatment to the density of bacteria before the treatment. Six biological replicates are shown. Experiments were repeated three times. **c**, In vitro anticancer effect of IDNP in a CRC cell–*F. nucleatum*–*C. butyricum* triple-culture system. Experiments were repeated three times. Six biological replicates are shown. **d**, TEM images of P2 phages (left), DNP (middle) and A-phage–D-IDNP assemblies (right), and analysis of the size of IDNPs using dynamic light scattering. Three images were captured for each group. Scale bars, 50 nm (left) and 500 nm (middle and right). **e**, Changes in the levels of *F. nucleatum* and *C. butyricum* in faecal samples collected from piglets that received phage and DNPs. Three biological replicates are shown. **f**, Biosafety study of phage and DNPs in piglets. Haematological examinations (left; leukocytes (WBC), erythrocytes (lymph), intermediate cells (mid), granulocytes (gran) and platelets (PLT)), liver function tests (second on the left; alanine aminotransferase (ALT), aspartic transaminase (AST) and γ-glutamyl transpeptidase (GGT)), kidney function tests (middle and second on the right; urea, glucose (GLU), creatinine (CRE) and bilirubin (TBIL)) and anaphylactic reaction measurements (right; IgG, IgE and histamine) were performed in piglets after receiving phages and DNPs. Three biological replicates are shown. Significance between two groups was calculated using two-tailed Student's *t*-tests (**a**, **e** and **f**) or one-way ANOVA with Tukey post hoc test (**b** and **c**). Data are mean ± s.d.

noted that the majority of these genes were associated with apoptosis and autophagy. The chemoresistance of CRC induced by *F. nucleatum* was found to result from the activation of anti-apoptosis pathways (Supplementary Fig. 5c); the elimination of these bacteria inhibited the expression of anti-apoptotic genes, such as

Csf2, *Bcl6* and *Mitf*. Furthermore, the upregulation of anti-autophagy genes (*Tspo*, *Poldip2* and *Akt11*) and the downregulation of pro-autophagy genes (*Lrrk2*, *Adrb2*, *Zc3h12a*, *Dram1* and *Dram2*) was observed after phage treatment (Fig. 2i). Transmission electron microscopy (TEM) images also revealed the same result, that is, a

morphology of autophagy could be observed in cancer cells that were treated with *F. nucleatum* (Fig. 2j). Thus, we speculated that *F. nucleatum* might prevent CRC cells from chemotherapy-induced apoptosis by protective autophagy. We also observed a number of bilayer vesicles (autophagosomes) that contained organelle debris in the cytoplasm—a typical feature of cell autophagy. By contrast, in cells treated with chemotherapy alone or with chemotherapy and phages, we observed morphological changes associated with apoptosis, including strong chromatin compaction and the formation of apoptotic bodies.

In agreement with the results described above, GFP–LC3 analysis and a western blot assay also indicated that *F. nucleatum* upregulated the expression of autophagy protein LC3-II (Supplementary Fig. 5d–g). Cells expressing mCherry–GFP–LC3 were also used to evaluate the induction of autophagy. The autophagic flux was determined by the ratio of GFP to mCherry using flow cytometry. An increased ratio of GFP–LC3:mCherry was found in cells treated with *F. nucleatum* (Supplementary Fig. 5e), whereas the addition of phages suppressed autophagy. We showed that 3-methyladenine (3-MA)—a broad spectrum inhibitor of autophagy—blocked the autophagic flux in cells treated with *F. nucleatum* and enhanced the therapeutic effect of chemotherapy (Fig. 2k). Furthermore, short interfering RNA (siRNA) against *Tlr4* and *MyD88* inhibited protective autophagy. Ac-DEVD-CHO (an inhibitor of apoptosis) was found to rescue CT26 cells from chemotherapy alone or from cell death induced by treatment with both chemotherapy and phages. Thus, it is now clear that the adhesion of *F. nucleatum* could induce protective autophagy in CRC cells through the TLR4–Myd88 signalling pathway[29,30]. A possible mechanism is shown in Fig. 2l. We speculate that the interaction of bacteria with TLR4 is an important step in triggering this effect. However, there may be other undiscovered interactions between *F. nucleatum* and colon cancer cells that could synergize with the TLR4 pathway to initiate protective autophagy.

A DNP that enhances the proliferation of *C. butyricum*

We investigated the anticancer mechanism of *C. butyricum*. As shown in Fig. 3a, the cytotoxicity was attributed to the secreta, as the BHI medium containing *C. butyricum* secreta exhibited strong cytotoxicity towards cancer cells. We also noticed that *C. butyricum* without its secreta showed negligible cytotoxicity towards CT26 cells. The lower molecular mass component (molecular mass < 3,000 Da) of the *C. butyricum* secreta was found to eliminate up to 50% of cancer cells. Gas chromatography–mass spectrometry (GC–MS) was used to determine the concentration of butyrate. The butyrate concentration of the *C. butyricum* secreta was estimated to be approximately 6.5 mM. Coincidentally, 6.5 mM of butyrate exhibited a similar effect of cytotoxicity towards CT26 cells. Furthermore, after the treatment with neutral red (NR)—an inhibitor of butyrate kinase—cytotoxicity of *C. butyricum* towards CT26 cells was significantly reduced. Taken together, we deduced that the anticancer effect of *C. butyricum* was mainly attributed to its capacity to secrete butyrate.

To screen for materials that are capable of promoting the growth of *C. butyricum* and delivering anticancer agents[31], eight types of nanoparticles were purchased or prepared (Supplementary Fig. 6a-c) and their effects on *F. nucleatum* and *C. butyricum* were tested. We observed that DNP significantly enhanced the cell proliferation of *C. butyricum*, whereas the growth of *F. nucleatum* remained unchanged (Fig. 3b). DNP incubation also enhanced the production of butyrate in *C. butyricum* (Supplementary Fig. 7a). Finally, IRT was encapsulated in the DNPs to form therapeutic IDNPs[32]. Treatment with phages and IDNPs showed a much greater anticancer effect compared with antibiotic therapy and chemotherapy (Fig. 3c). Although antibiotics were effective at inhibiting *F. nucleatum* and at improving the therapeutic effect of IDNPs, the undesired side effect that *C. butyricum* was also killed caused a reduction in the level of butyrate-induced cytotoxicity. By contrast, neither DNPs nor phages showed significant cytotoxicity to cancer cells (Supplementary Fig. 7c).

TEM images of P2 phages, D-IDNPs and bioorthogonally conjugated A-phage–D-IDNP assemblies are shown in Fig. 3d. IDNP was confirmed to have an average size of 310 nm, as determined by dynamic light scattering. According to morphological classification and molecular-biology analysis, we speculate that P2 phages were dsDNA viruses belonging to the order of Caudovirales.

Biosafety research in piglets

Piglets and humans have a similar gastrointestinal structure and gut microbiota[33]. We evaluated the biocompatibility of phages and DNPs in Bama minipiglets (*Sus scrofa*). Decreased levels of *F. nucleatum* and increased levels of *C. butyricum* were found in piglets 7 d after oral administration of phage and DNP (Fig. 3e). Negligible changes could be found in both total and differential haemocyte counts (including leukocytes, erythrocytes, intermediate cells, granulocytes and platelets; Fig 3f). Liver functions (alanine aminotransferase, aspartic transaminase and γ-glutamyl transpeptidase) and renal functions (urea, creatinine and bilirubin) were also assessed. Biochemical examination of blood from the piglets showed no significant variation over time. Constant levels of blood immunoglobulin E (IgE), immunoglobulin G (IgG) and histamine levels in piglets indicated that phages and DNPs had a low risk of inducing allergic symptoms. These results suggest that this therapy would be appropriate for large animals and humans.

Fig. 4 | A-phage-mediated tumour targeting. a, Illustration of the tumour-targeting mechanism of A-phages and D-IDNPs. After treatment with the amino acid analogue L-azidohomoalanine, *F. nucleatum* uses the L-azidohomoalanine to synthesize proteins. The capsid proteins of phages were then modified with the azide group. After intragastrical administration of the A-phages, the phages bind to *F. nucleatum* in the tumour tissue. The DBCOs in D-IDNPs and the azide groups in A-phages undergo copper-free cycloaddition, forming a covalently linked product that accumulates in the tumour. **b**, Fluorescence imaging of the efficiency of bioorthogonal binding between A-phages and D-IDNPs. Through the covalent link between DBCO and azide groups, D-IDNPs tended to bind to A-phages immobilized in hydrogel. Three biological replicates are shown. **c**, In vitro binding effect of A-phages and D-IDNPs in a flow environment (viscosity, 35 cP; speed, 0.85 cm s⁻¹). A-phages could selectively bind to the hydrogel containing *F. nucleatum* but not to the hydrogel containing *E. coli*. Using bioorthogonal chemistry, D-IDNPs could covalently link to the hydrogel with A-phage accumulation but not to the phage-containing hydrogel. Images are representative of three biological replicates. **d**, In vivo fluorescence imaging showing the capacity of A-phages to guide tumour-specific accumulation of D-IDNPs. Mice were intragastrically administered with A-phages and the biodistribution of these A-phages was observed at the indicated time points. The pretargeted A-phages guided the accumulation of D-IDNPs (15 min after intragastric administration) through bioorthogonal chemistry. Images are representative of three biological replicates. The tumours at the 24 h time point are indicated by circles. **e**, Ex vivo fluorescence imaging of the intratumoural accumulation of D-IDNPs 24 h after intravenous injection of D-IDNPs. Images are representative of three biological replicates. Circles indicate tumours. **f**, Quantitative analysis of intratumoural accumulation of phages and nanoparticles. The intratumoural fluorescence intensity of Cy5 was measured in A-phages and in tumours treated with phages. The intratumoural fluorescence intensity of IR808 was measured in tumours treated with either A-phages and D-IDNPs, or phages and IDNP. Four biological replicates are shown. Significance between the two groups was calculated using two-tailed Student's *t*-tests (**b**, **c** and **f**). Data are mean ± s.d.

We also investigated the storage condition of phages and IDNPs. IDNPs were stored as a lyophilized powder, and phages were dispersed in stock solution. After storage at 4 °C for three months, the activity of these agents remained unchanged (Supplementary Fig. 8a–d). A limited increase in bacterial endotoxin could be detected by the Limulus test under these storage conditions (Supplementary Fig. 8e,f). The ability of phages to target tumours colonized with *F. nucleatum* and the ability of DNP nanoparticles to

enhance the growth of *C. butyricum* were not affected after storage for six months (Supplementary Fig. 8g–i). By contrast, the enrichment of phages in tumours was very low in mice without colonization with *F. nucleatum*.

Tumour-targeting effects

To improve the therapeutic performance and reduce the side effects of IDNPs, we used a bioorthogonal reaction to achieve phage-guided
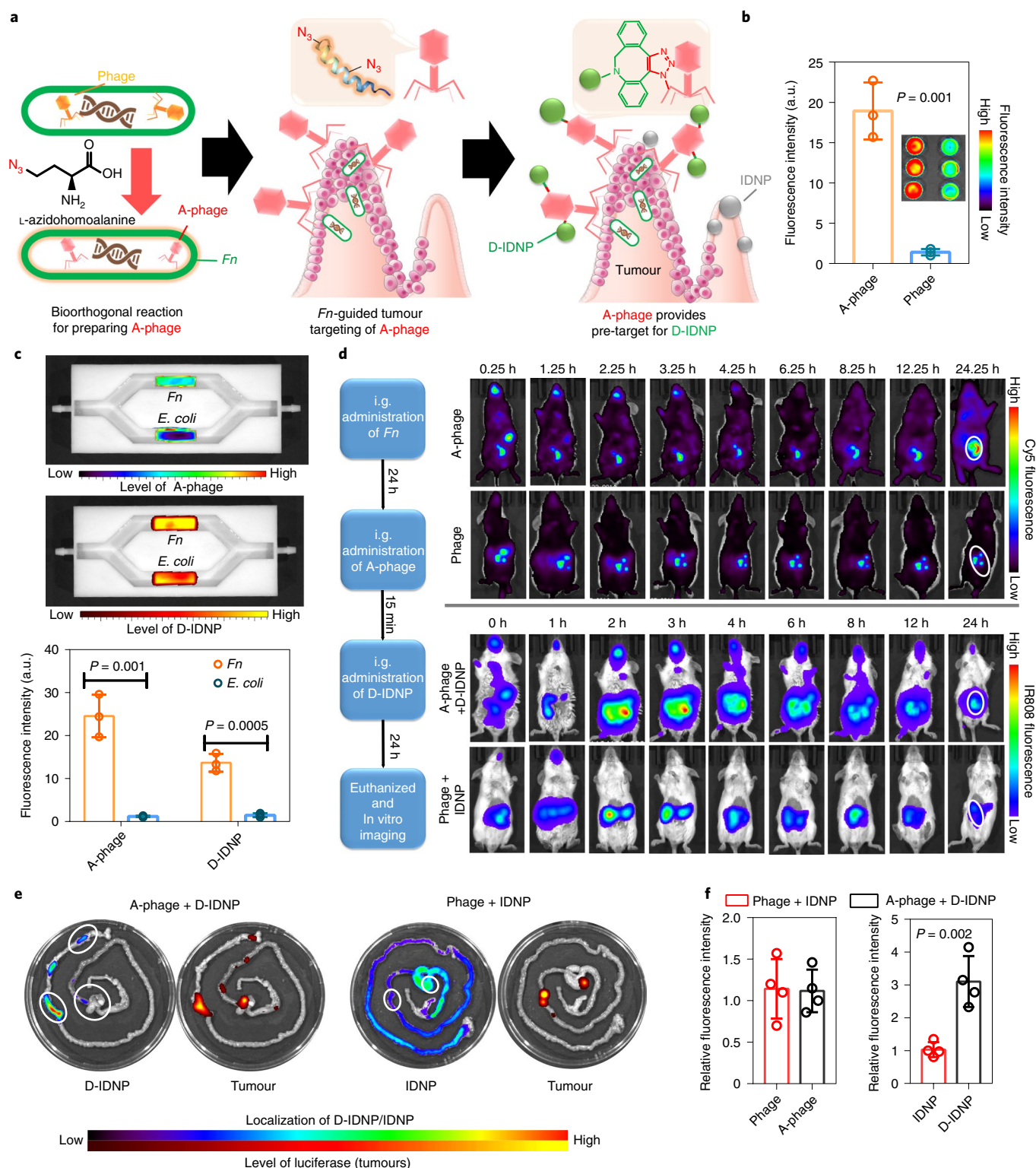
tumour targeting (Fig. 4a). To obtain A-phages, L-azidohomoalanine was added to the culture medium of phage-infected *F. nucleatum*[34]. Using 1-ethyl-3-(3-dimethyl aminopropyl) carbodiimide (EDC)–*N*-hydroxysuccinimide (NHS)-coupling chemistry, DBCO-NH$_2$ was conjugated with IDNPs to obtain D-IDNPs. This chemical modification did not alter the growth-promoting effect of the IDNPs towards *C. butyricum* (Supplementary Fig. 8j). As a comparison, wild-type phages or A-phages were immobilized in hydrogels and mixed with D-IDNPs. A much stronger fluorescence signal for D-IDNPs was observed in A-phage-immobilized hydrogels, indicating the facilitative effect of the bioorthogonal reaction under static conditions (Fig. 4b).

To study whether D-IDNPs could be covalently linked to A-phages in a flow environment, we designed and fabricated a circulating system to simulate the condition of intestinal juice flow (Fig. 4c, Supplementary Fig. 9a). *E. coli* or *F. nucleatum* were immobilized in an agarose hydrogel cuboid. The hydrogels containing *E. coli* or *F. nucleatum* were inserted into two grooves of this device. The simulated intestinal juice containing RhB-labelled A-phages was then circulated in the circulating device at a physical-flow speed. The red fluorescence of A-phages accumulated in the *F. nucleatum*-immobilized gel. By contrast, limited fluorescence was observed in the hydrogel containing *E. coli* (Fig. 4c). After the circulating fluid was replaced with simulated intestinal juice containing IR808-labelled D-IDNPs, notable levels of IR808 fluorescence accumulation could still be observed after 6 h of circulation (Fig. 4c). The *F. nucleatum*-specific accumulation of D-IDNPs was mediated by the interactions between phages and bacteria. The bioorthogonal linkage between A-phages and D-IDNPs was also efficient in this simulated intestinal environment.

The capacity of the phage-guided nanotherapeutic system to target tumours was studied in a luciferase-expressing orthotopic CT26 (CT26[luc]) model (Fig. 4d). Phages (wild-type or A-phages) and therapeutic agents (IDNPs or D-IDNPs) were given sequentially 24 h after the colonization of *F. nucleatum*. Through binding to *F. nucleatum*, these phages were found to enter the intestine and to accumulate in the tumour. As DBCO and azide could undergo a copper-free cycloaddition to obtain a covalently linked product, most D-IDNPs accumulated in the tumour. By contrast, very limited overlap between IDNPs and transplanted tumours was found. D-IDNPs were found to specifically locate in tumour nodules of the intestinal tract (Fig. 4e). Instead, a relatively uniform distribution of fluorescence within the entire digestive tract could be observed in IDNP-treated mice. Quantitatively, the bioorthogonal-chemistry strategy increased the tumour accumulation of IDNPs by

approximately threefold (Fig. 4f). The M13 phage-based nanosystem showed negligible targeting (Supplementary Fig. 10a).

We also show the ability of this pretargeting strategy in reducing the side effects of chemotherapy. Using haematoxylin and eosin (H&E) staining, common features of intestinal mucositis—including short villi, partial crypt necrosis and the presence of enterocyte vacuolization—were observed in the IRT and IDNP groups (Supplementary Fig. 10b–e). By contrast, treatment with both A-phages and D-IDNPs offered a significant level of protection for normal tissues against the side effects induced by chemotherapy.

In vivo anticancer studies

To study the capacity of this therapy in reversing chemoresistance mediated by *F. nucleatum*, we peritumourally injected these agents into a subcutaneous tumour model. After 14 d, the IDNP treatment only suppressed around 30% of tumour growth, whereas the combination with phages displayed a tumour-inhibition rate of 62% (Supplementary Fig. 11a–c).

CT26[luc] cells were then implanted into the caecum of BALB/c mice, and various treatments were performed on the mice (Fig. 5a). Growth of the tumour was monitored through the bioluminescence of cancer cells (Fig. 5b). The mice treated with both A-phages and D-IDNPs displayed the smallest tumour volume and the weakest intensity of bioluminescence. By contrast, mice treated with FOLFIRI (5-fluorouracil, leucovorin and IRT combination therapy) or monotherapy (IRT or IDNP) exhibited a modest delay in tumour growth compared with the PBS-treated control. Interestingly, the antibiotic cocktail of metronidazole, vancomycin and ampicillin was found to suppress tumour growth to some extent; however, this treatment had no effect on prognosis.
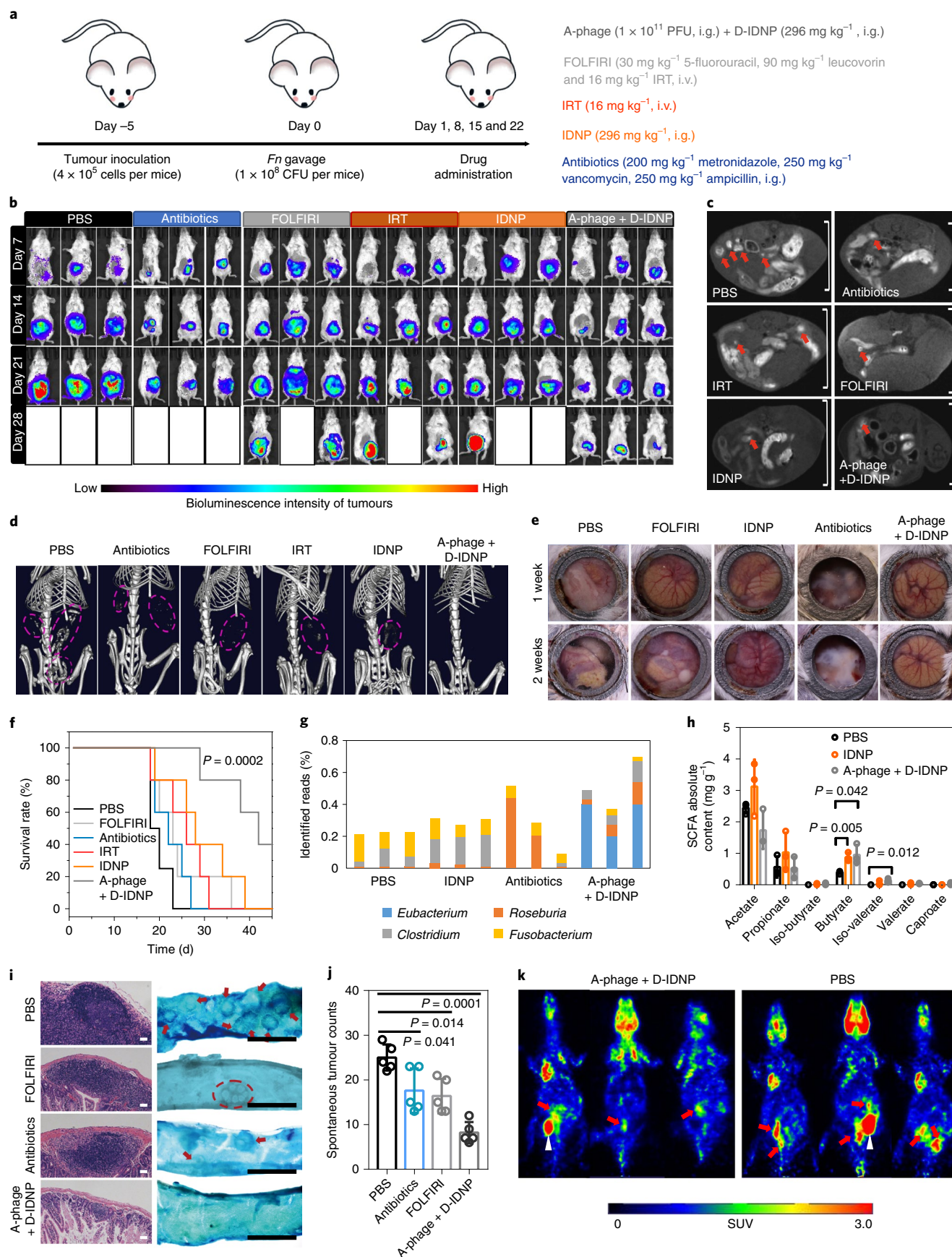
Both magnetic resonance imaging (MRI) and computed tomography (CT) imaging were performed to assess the effects of these therapies. On images of T1-weighted MRIs, suspected tumours with an enhanced rim in the descending colon could be clearly observed (Fig. 5c). In the group treated with both A-phage and D-IDNP, the volume of primary tumours was relatively small. By contrast, rapid tumour growth, together with enhanced tumour invasion, was found in other groups (Supplementary Fig. 12a–c). This result was also confirmed by CT scanning; suspected tumour invasions could be observed in mice after receiving other treatments (Fig. 5d).

We developed an abdominal imaging window using 3D printing for the long-term observation of the development of CRC[35]. As shown in Fig. 5e, mice that received PBS or the antibiotic cocktail showed rapid tumour growth, and a tumour mass with greyish-white colour appeared one to two weeks after inoculation. However,

---

Fig. 5 | Anticancer effects in mice bearing luciferase-expressing orthotopic CT26 tumours and in C57BL/6J *Apc*[Min/+] mice developing spontaneous colonic tumours. a–g, Results for the mice bearing orthotopic CT26[luc] tumours. **a**, Timeline of treatments of mice with orthotopic CT26 tumours. PFU, plaque forming units. **b**, In vivo bioluminescence imaging of the mice after receiving PBS, antibiotics, FOLFIRI, IRT, IDNPs, and both A-phages and D-IDNPs. Three representative mice are shown for each treatment group. White boxes denote dying mice. The therapeutics were administered once per week. **c**, T1 MRI imaging at day 14. The orthotopic tumours (high signal intensity) grown along the intestinal wall displayed an invasive character. One mouse per treatment group is shown. Red arrows indicate suspected tumour nodes. Scale bars, 2 cm. **d**, CT scanning of tumour-bearing mice at day 14. One mouse per treatment group is shown. The dashed circles indicate abnormal areas. **e**, Abdominal imaging window for the long-term observation of the therapeutic effects. The windows (with a inner diameter of 1 cm) were surgically implanted into the abdomen of the mice before the various treatments. Tumour growth was directly observed with a stereomicroscope in situ. Images are representative of three biological replicates. The tumour mass had a greyish-white colour. **f**, Survival graph of the tumour-bearing mice (*n* = 6 for the PBS group and *n* = 5 for the other groups). **g**, Changes in gut microbiota after the treatments. The identified reads of each bacteria and total sequenced 16S rDNA were compared. Three biological replicates are shown. Sequencing was performed at day 14. **h**, Faecal SCFA levels after the different treatments. Three biological replicates are shown. GC–MS analysis was performed to analyse faecal SCFA levels at day 8. **i**, H&E staining and microscopy images of spontaneous tumours in *Apc*[Min/+] mice after treatment on day 60. One mouse per treatment group is shown. The arrows and dashed circles indicate the spontaneous tumours. The therapeutic agents were administered once per week. Left scale bars, 100 μm; right scale bars, 5 mm. **j**, Numbers of spontaneous tumours in *Apc*[Min/+] mice after treatment. The number of tumours was determined using a stereomicroscope. Five biological replicates are shown. **k**, ^{18}F-FDG-PET imaging of *Apc*[Min/+] mice eight weeks after the initial treatment with PBS or both A-phage and D-IDNP. Three biological replicates are shown. Red arrows indicate suspected tumour nodes. White arrows indicate bladders. SUV, standard uptake value. Significance between two groups was calculated using one-way ANOVA with Tukey's post hoc test (**h** and **j**) or Mantel–Cox tests (**f**). Data are mean ± s.d.

no obvious tumour mass could be observed in mice treated with both A-phage and D-IDNP. Treatment with FOLFIRI or IDNP suppressed the development of tumours to some extent; however, rapidly growing tumour tissues were still found two weeks after tumour implantation. This result was also corroborated by histological analysis (Supplementary Fig. 12c). The median survival of

a A-phage (1×10^{11} PFU, i.g.) + D-IDNP (296 mg kg^{-1}, i.g.)

FOLFIRI (30 mg kg^{-1} 5-fluorouracil, 90 mg kg^{-1} leucovorin and 16 mg kg^{-1} IRT, i.v.)

IRT (16 mg kg^{-1}, i.v.)

IDNP (296 mg kg^{-1}, i.g.)

Antibiotics (200 mg kg^{-1} metronidazole, 250 mg kg^{-1} vancomycin, 250 mg kg^{-1} ampicillin, i.g.)

Day −5 — Tumour inoculation (4×10^5 cells per mice)

Day 0 — *Fn* gavage (1×10^8 CFU per mice)

Day 1, 8, 15 and 22 — Drug administration

b PBS | Antibiotics | FOLFIRI | IRT | IDNP | A-phage + D-IDNP

Day 7 / Day 14 / Day 21 / Day 28

Low — High — Bioluminescence intensity of tumours

c PBS | Antibiotics | IRT | FOLFIRI | IDNP | A-phage +D-IDNP

d PBS | Antibiotics | FOLFIRI | IRT | IDNP | A-phage + D-IDNP

e PBS | FOLFIRI | IDNP | Antibiotics | A-phage + D-IDNP — 1 week / 2 weeks

f Survival rate (%) vs Time (d); $P = 0.0002$; PBS, FOLFIRI, Antibiotics, IRT, IDNP, A-phage + D-IDNP

g Identified reads (%); PBS, IDNP, Antibiotics, A-phage + D-IDNP; Eubacterium, Roseburia, Clostridium, Fusobacterium

h SCFA absolute content (mg g^{-1}); PBS, IDNP, A-phage + D-IDNP; Acetate, Propionate, Iso-butyrate, Butyrate, Iso-valerate, Valerate, Caproate; $P = 0.042$, $P = 0.005$, $P = 0.012$

i PBS, FOLFIRI, Antibiotics, A-phage + D-IDNP

j Spontaneous tumour counts; PBS, Antibiotics, FOLFIRI, A-phage + D-IDNP; $P = 0.0001$, $P = 0.014$, $P = 0.041$

k A-phage + D-IDNP | PBS; SUV 0 – 3.0

mice treated with both A-phage and D-IDNP was increased from 20 d in the PBS-treated mice to 42 d (Fig. 5f).

Next, we analysed changes in the composition of intestinal microbiota after various therapies. Mice treated with both A-phage and D-IDNP exhibited a significant decrease in the numbers of *F. nucleatum* ($P = 0.01$; Fig. 5g, Supplementary Figs. 13 and 14a–e). Furthermore, enhanced growth of butyrate-producing microbiota was correlated with the use of DNPs ($P = 0.0009$). GC–MS analysis was conducted to measure colonic SCFA levels after treatment. Using faecal metabolomics analyses, we observed significantly increased concentrations of butyrate in mice treated with both A-phage and D-IDNP (Fig. 5h). Taken together, the administration of both A-phages and D-IDNPs led to a highly regulated gut microbiota, resulting from the elimination of pro-tumoural *F. nucleatum* and the promotion of the growth of anti-tumoural butyrate-producing bacteria.

As the pathogenesis of *Apc*[Min/+] mice was similar to that in humans, we also investigated the therapeutic effect of administering both A-phages and D-IDNPs in transgenic *Apc*[Min/+] mice. After eight weeks of therapy, mice were euthanized and their intestinal tracts were collected. Using H&E staining, we showed that adenomas in the PBS group had the largest size, and that adenomas were rarely found in the group treated with both A-phage and D-IDNP. To visualize the adenomas in intestinal tracts, methylene-blue staining was performed. Microscopy examination showed that the *Apc*[Min/+] mice in the PBS group developed more than 20 adenomas (Fig. 5i,j, Supplementary Fig. 15c). By contrast, only 8.2 adenomas could be found in the intestinal tract of mice treated with both A-phage and D-IDNP. Treatment with FOLFIRI or antibiotics slightly inhibited the development of CRC. Moreover, we used small-animal positron emission tomography with fluorine-18 fluorodeoxyglucose (^{18}F-FDG PET) to identify unsuspected tumour growth (Fig. 5k). Visual analysis of the PET scans showed abdominal hot spots in segments of the small intestine and colons that correlated with the existence of intestinal adenomas. In the PBS group, ^{18}F-FDG PET images displayed several strong abdominal signal spots in each mouse, indicating the existence of intestinal adenomas. The accumulation of abdominal ^{18}F-FDG correlated with the number of adenomas[36]. For the *Apc*[Min/+] mice treated with both A-phages and D-IDNPs, we observed a reduction in the accumulation of abdominal ^{18}F-FDG.

Outlook

We have shown that a biotic–abiotic hybrid nanosystem can augment the effects of chemotherapy for CRC by the modulation of the gut microbiota. In dosage forms of lyophilized powder (for the D-IDNPs) and stock solution (for the A-phages), the bioactivity of the system could be maintained for up to three months when refrigerated, which should facilitate further studies. Overall, targeting the communication between commensal microbiota and host cells should not be restricted to gastrointestinal tumours and could be adapted to diseases associated with other organs.

Methods

Cell lines. HT29 cells, HCT116 cells and CT26 cells were obtained from the China Centre for Type Culture Collection. CT26 cells were cultured in Roswell Park Memorial Institute 1640 medium (Gibco, Invitrogen) supplemented with 10% fetal bovine serum (Invitrogen), 100 U ml^{−1} penicillin (Invitrogen) and 100 U ml^{−1} streptomycin (Invitrogen), and incubated at 37 °C with 5% CO_2. HCT116 and HT29 cells were cultured in McCoy's 5A medium supplemented with 10% fetal bovine serum (Invitrogen), 100 U ml^{−1} penicillin (Invitrogen) and 100 U ml^{−1} streptomycin (Invitrogen) and incubated at 37 °C with 5% CO_2. Low-passage cells (5th to 25th passage) were used for the experiments.

Bacterial strains. *F. nucleatum* (ATCC 10953, ATCC 25586, ATCC 23726, VPI 4351 and ATCC 49256), *B. subtilis* (ATCC 6051), *B. thuringiensis* (ATCC 10792), *E. coli* (MG1655) and *C. butyricum* (ATCC 19398) strains were obtained from the American Type Culture Collection (ATCC). Unless otherwise stated,

F. nucleatum (ATCC 10953) and *C. butyricum* (ATCC 19398) were used for bacterial experiments. BHI broth (Qingdao Hope Biotechnology) and Luria–Bertani (LB) broth were used for bacterial culture.

Synthesis of DNPs. To synthesize DNPs, 0.6 g 2-nitroimidazole (NI) and 1.1 g K_2CO_3 were dissolved in dimethyl formamide (DMF). Then, 1.56 g 6-(Boc-amino) hexyl bromide in DMF was added dropwise and stirred at room temperature for 24 h. After evaporation, the mixture was filtered and washed with methanol. The solid was suspended in water and extracted with ethyl acetate. The organic layer was separated, dried with sodium sulfate and concentrated to obtain the product. The resulting product was dissolved in methanol and cooled to 0 °C, and 10 ml of 1.25 M HCl in methanol was added. The solution was then stirred at room temperature for 24 h. The solvent was removed using a rotary evaporator to obtain NI derivative. Next, 0.3 g carboxymethyl-dextran sodium salt, 2 g EDC and 1.26 g NHS were dissolved in DMF and stirred for about 15 min. Then, 0.2 g NI derivative in DMF was added slowly and stirred for 24 h. The product was dialysed against water to remove by-products to obtain purified NI–dextran.

Drug loading and release of IRT from IDNP. IRT was loaded into DNP by hydrophobic interaction. Then, 30 mg NI-dextran was dissolved in ultrapure water and 3 mg IRT in dichloromethane (DCM) was added dropwise to the above solution. The mixture was stirred overnight and dialysed to remove unloaded IRT. Finally, the solution was lyophilized to obtain IDNP. The encapsulation efficiency was determined by the disruption of IDNP using dimethyl sulfoxide (DMSO), and the fluorescence intensity of IRT (excitation at 390 nm, emission at 460 nm) was measured.

Synthesis of D-DNP. To synthesize D-DNP, 50 mg DNP was resuspended in ultrapure water, to which 35 mg EDC and 21 mg NHS were added and stirred for 15 min. Then, 20 mg DBCO-PEG_{2000}-NH_2 was dissolved in ultrapure water and added to the above reaction mixture while stirring at room temperature overnight. The obtained reaction mixture was dialysed against ultrapure water for 1 d.

Phage screening. Faeces from male C57BL/6J *Apc*[Min/+] mice and saliva samples from humans were collected and used for phage screening; 20 mg faeces was collected from eight-week-old *Apc*[Min/+] mice. Faecal samples were then homogenized in 4 ml of BHI medium and centrifuged for 5 min at 3,920g. The supernatant was filtered through Millex-GV 0.45 μm pore size aqueous filters (Millipore). The solution was then mixed with 5 ml *F. nucleatum* (optical density at 600 nm (OD_{600}) = 0.3) and added to 20 ml BHI broth for overnight incubation at 37 °C. The mixture was subsequently centrifuged at 3,920g for 5 min at 4 °C. After three rounds of screening, the mixture was obtained and phages were isolated and purified using the double-layer method. Similarly, saliva of healthy individuals was collected for phage screening. All of the samples were centrifuged for 5 min at 3,920g and the supernatant was filtered (using a 0.45 μm filter). Then, 10 μl of these saliva samples was incubated with 5 ml *F. nucleatum* in 20 ml BHI broth (OD_{600} = 0.3) in anaerobic conditions at 37 °C overnight. The mixture was then centrifuged for 5 min at 3,920g and 4 °C, and the supernatant was filtered through 0.45 μm filters. After three rounds of screening, phages were isolated and purified using the double-layer method.

Isolation of phages. Phages were individually diluted 10[6]-fold, 10[7]-fold and 10[8]-fold. At the same time, agarose top medium (0.7% agarose in LB) was dispensed into sterile culture tubes to dilute phages. Tubes were equilibrated at 45 °C until ready for use. Then, 100 μl mid-log phase *F. nucleatum* was mixed with 100 μl of diluted phages for about 5 min and the mixture was added to melted agarose. The infected bacterial cells were immediately poured onto a prewarmed BHI plate, and the agarose top medium was spread among the plate using the tilting-plate method. Plates were placed in anaerobic conditions at 37 °C. Subsequently, 5 μl of the phage suspension was spotted on the plate. The lysis plaques showed a heterogeneous morphology with a diameter of approximately 2 mm and this procedure was repeated three times. The clearest plaque was then picked and propagated and a lysate was obtained and preserved at 4 °C for further study.

Purification of bacteriophages DNA and restriction analysis. Phage DNA was isolated from 50 ml lysate by QIAprep Spin Miniprep Kit. Different kinds of restriction enzymes, including DNase, RNase, HindIII, XbaI, EcoR1, BamHI, KpnI, XbaI, XhoI, ApaI, NheI and SacI, were used to test the susceptibility of the nucleic acids. Electrophoresis of these products was performed at 100 V for 1 h in 1% agarose gel in Tris-acetate buffer.

Antibacterial effect of phages. Cultures of *B. subtilis*, *B. thuringiensis*, *E. coli*, *C. butyricum* and various *F. nucleatum* strains in exponential growth were co-inoculated with P1 or P2 at a multiplicities of infection (MOI) of 0.1. The mixture was incubated and the OD_{600} was measured over time to monitor the antibacterial effects of these two types of phages.

Nanoparticles screening. Eight types of nanoparticle (AuNP, Fe_3O_4, C_3N_4, cellulose, graphene, ZnO, AgNP and dextran) were individually co-cultured with *F. nucleatum* (10[5] CFU ml^{−1}) and *C. butyricum* (10[5] CFU ml^{−1}). The OD_{600} was measured to monitor the growth of bacteria.

In vitro phage-binding assay using various strains of bacteria. The tissue microarray was purchased from Biomax. All human tissues were collected using protocols that were approved by Institutional Review Board and Health Insurance Portability and Accountability Act. All animal tissues were collected using Institutional Animal Care and Use Committee (IACUC)-approved protocols. All samples tested negative for HIV and hepatitis B, or their counterparts in animals, and were approved for commercial product development. *F. nucleatum* (10^8 CFU ml^{-1}), *B. thuringiensis* (10^8 CFU ml^{-1}), *E. coli* (10^8 CFU ml^{-1}) and *C. butyricum* (10^8 CFU ml^{-1}) were labelled with green fluorescent FITC. Meanwhile, phages were marked with red fluorescent rhodamine B. Bacteria were then co-incubated with phages for 30 min. The binding process was observed using a super-resolution fluorescence microscopy (Leica TCS SP8 STED).

Cytotoxicity of *F. nucleatum* and *C. butyricum*. The biological effects of *F. nucleatum* and *C. butyricum* on colorectal cancer cell lines were examined by 3-(4,5-Dimethylthiazol-2-yl)-2,5-diphenyltetrazolium bromide (MTT) assay. CT26 cells, HT29 cells and HCT116 cells were seeded on 24-well plates with a density of 1×10^5 cells per well. *F. nucleatum* (1×10^7 CFU per well) and *C. butyricum* (1×10^7 CFU per well) were co-cultured with various CRC cell lines for 48 h. MTT (5 mg ml^{-1}) was then added into each well and co-incubated with cancer cells for another 4 h. The cultured medium of each well was replaced with DMSO. The OD$_{570}$ was measured using a SpectraMax i3x multi-mode detection platform.

In vitro anticancer effects. CT26 cells, HT29 cells and HCT116 cells were seeded on 24-well plates (1×10^5 cells per well). After being individually treated with PBS, IDNP (30 μM), IDNP (30 μM) and *F. nucleatum* (1×10^7 CFU), or phage and IDNP (30 μM IDNP, 1×10^7 CFU *F. nucleatum* and 1×10^8 PFU phage), the cancer cells were incubated for another 48 h. The MTT solution (5 mg ml^{-1}) was added into each well and the OD$_{570}$ was measured for each well. The anticancer efficacy of both phage and IDNP was investigated in a triple-culture system with CT26 cells, *F. nucleatum* and *C. butyricum*. CT26 cells (1×10^5 cells per well) were seeded in a 24-well plate (Corning Costar) and different treatments were conducted. *F. nucleatum* (1×10^7 CFU per well) was co-cultured with CT26 cells in the bottom chamber, and *C. butyricum* (1×10^7 CFU per well) was placed in the top chamber of the assay. *F. nucleatum* was pretreated by co-incubation with antibiotics (50 μM metronidazole). After co-incubation for 48 h, MTT assays were used to evaluate the cytotoxicity.

In vivo anticancer therapy in various mouse models. Experimental protocols were approved by the IACUC of the Animal Experiment Center of Wuhan University. All animal experimental procedures were performed in accordance with the Regulations for the Administration of Affairs Concerning Experimental Animals approved by the State Council of China. The therapeutic effect of both A-phage and D-IDNP was assessed in a subcutaneous CT26 tumour model, in an orthotopic implantation CRC model and in C57BL/6J *Apc*$^{Min/+}$ mice.

CT26 cells (100 μl, 1×10^7 cells ml^{-1}) were subcutaneously injected into the right flank of BALB/c mice. When tumours reached an approximate size of 100 mm^3, mice were randomly divided into four groups with five mice in each group for different sets of experiments. *F. nucleatum* was given by multipoint intratumoural injection twice per week for three weeks. PBS (100 μl), phages (100 μl, 1×10^{11} PFU), IDNP (100 μl, 296 mg kg^{-1}), and IDNPs (100 μl, 296 mg kg^{-1}) and phages (100 μl, 1×10^{11} PFU) were subcutaneously injected into the tumours of mice in each of the four groups. These agents were given to the mice on day 1 of the experiment, in which day 0 was defined as the first day of *F. nucleatum* administration. Tumour volumes were recorded every 2 d and calculated as $V = 0.5 \times L \times W^2$ where L and W are the longest and the shortest lengths of the tumour, respectively.

In the orthotopic implantation model, luciferase-transfected CT26 cells (40 μl per mice, 1×10^7 cells ml^{-1}) were implanted into the caecum of BALB/c mice. The growth of the orthotopic tumours was observed through the bioluminescence of cancer cells using an IVIS (Perkin Elmer) system. Mice were gavaged with 1×10^8 CFU *F. nucleatum* on day 0, and randomly divided into six groups with five mice in each group. Then, 100 μl PBS, 100 μl antibiotic cocktail (200 mg kg^{-1} metronidazole, 250 mg kg^{-1} ampicillin, 250 mg kg^{-1} vancomycin), 100 μl IDNPs (296 mg kg^{-1}), and A-phages and D-IDNPs (100 μl D-IDNP, 296 mg kg^{-1} and 100 μl A-phage, 1×10^{11} PFU) were intragastrically administered every week. For mice in the FOLFIRI group and the IRT group, 100 μl of chemotherapeutics (30 mg kg^{-1} 5-fluorouracil, 90 mg kg^{-1} leucovorin and 16 mg kg^{-1} IRT by intravenous injection) and IRT (16 mg kg^{-1} by intravenous injection) were given once per week, respectively. Tumours and organs were collected for further pathologic analysis from mice that were euthanized after the end of the experiment and from mice that died during the experiment.

The therapeutic efficiency of the combined treatment with A-phages and D-IDNPs was also evaluated in C57BL/6J *Apc*$^{Min/+}$ mice. Mice (male, eight weeks old) were randomly divided into four groups with five mice in each group. All treatments were consistent with the orthotopic implantation model (dose and method of administration). At the end of the therapy, mice were euthanized and intestinal samples were collected for histological analysis. The levels of *F. nucleatum*

were qualitatively measured using FISH staining and quantitatively analysed using PCR. Abundance of other bacteria was analysed by 16S rDNA sequencing.

Reporting Summary. Further information on research design is available in the Nature Research Reporting Summary linked to this article.

Data availability
The authors declare that the main data that support the results of this study are available within the paper and the Supplementary Information. The raw and analysed datasets generated during the study are available for research purposes from the corresponding author on reasonable request.

References
1. Tremaroli, V. & Bäckhed, F. Functional interactions between the gut microbiota and host metabolism. *Nature* **489**, 242–249 (2012).
2. Schroeder, B. & Bäckhed, F. Signals from the gut microbiota to distant organs in physiology and disease. *Nat. Med.* **22**, 1079–1089 (2016).
3. Nicholson, J. K. et al. Host-gut microbiota metabolic interactions. *Science* **336**, 1262–1267 (2012).
4. van Nood, E. et al. Duodenal infusion of donor feces for recurrent *Clostridium difficile*. *N. Engl. J. Med.* **368**, 407–415 (2013).
5. Dewint, P. et al. Adalimumab combined with ciprofloxacin is superior to adalimumab monotherapy in perianal fistula closure in Crohn's disease: a randomised, double-blind, placebo controlled trial. *Gut* **63**, 292–299 (2014).
6. Vieira, S. M. Translocation of a gut pathobiont drives autoimmunity in mice and humans. *Science* **359**, 1156–1161 (2018).
7. Wang, Z. N. et al. Gut flora metabolism of phosphatidylcholine promotes cardiovascular disease. *Nature* **472**, 57–63 (2011).
8. Sears, C. L. & Garrett, W. S. Microbes, microbiota, and colon cancer. *Cell Host Microbe* **15**, 317–328 (2014).
9. Gopalakrishnan, V. et al. Gut microbiome modulates response to anti-PD-1 immunotherapy in melanoma patients. *Science* **359**, 97–103 (2018).
10. Geller, L. T. et al. Potential role of intratumor bacteria in mediating tumor resistance to the chemotherapeutic drug gemcitabine. *Science* **357**, 1156–1160 (2017).
11. Zheng, D. W. et al. Optically-controlled bacterial metabolite for cancer therapy. *Nat. Commun.* **9**, 1680 (2018).
12. Fan, J. X. et al. Bacteria-mediated tumor therapy utilizing phothermally-controlled TNF-α expression via oral administration. *Nano Lett.* **18**, 2373–2380 (2018).
13. Louis, P., Hold, G. L. & Flint, H. J. The gut microbiota, bacterial metabolites and colorectal cancer. *Nat. Rev. Microbiol.* **12**, 661–672 (2014).
14. Kostic, A. D. et al. *Fusobacterium nucleatum* potentiates intestinal tumorigenesis and modulates the tumor-immune microenvironment. *Cell Host Microbe* **14**, 207–215 (2013).
15. Mima, K. et al. *Fusobacterium nucleatum* and T cells in colorectal carcinoma. *JAMA Oncol.* **1**, 653–661 (2015).
16. Yu, T. C. et al. *Fusobacterium nucleatum* promotes chemoresistance to colorectal cancer by modulating autophagy. *Cell* **170**, 548–563 (2017).
17. Singh, N. et al. Activation of Gpr109a, receptor for niacin and the commensal metabolite butyrate, suppresses colonic inflammation and carcinogenesis. *Immunity* **40**, 128–139 (2014).
18. Cani, P. D. & Jordan, B. F. Gut microbiota-mediated inflammation in obesity: a link with gastrointestinal cancer. *Nat. Rev. Gastroenterol. Hepatol.* **15**, 671–682 (2018).
19. Bullman, S. et al. Analysis of *Fusobacterium* persistence and antibiotic response in colorectal cancer. *Science* **358**, 1443–1448 (2017).
20. Kelly, C. J. et al. Crosstalk between microbiota-derived short-chain fatty acids and intestinal epithelial HIF augments tissue barrier function. *Cell Host Microbe* **17**, 662–671 (2015).
21. Agarwal, R. et al. Inhaled bacteriophage-loaded polymeric microparticles ameliorate acute lung infections. *Nat. Biomed. Eng.* **2**, 841–849 (2018).
22. Citorik, R. J., Mimee, M. & Lu, T. K. Sequence-specific antimicrobials using efficiently delivered RNA-guided nucleases. *Nat. Biotechnol.* **32**, 1141–1145 (2014).
23. Hussain, S. et al. Antibiotic-loaded nanoparticles targeted to the site of infection enhance antibacterial efficacy. *Nat. Biomed. Eng.* **2**, 95–103 (2018).
24. Maslowski, K. M. & Mackay, C. R. Diet, gut microbiota and immune responses. *Nat. Immunol.* **12**, 5–9 (2011).
25. Wang, H. et al. Selective in vivo metabolic cell-labeling-mediated cancer targeting. *Nat. Chem. Biol.* **13**, 415–424 (2017).
26. Yu, J. et al. Metagenomic analysis of faecal microbiome as a tool towards targeted non-invasive biomarkers for colorectal cancer. *Gut* **66**, 70–78 (2017).

27. Arthur, J. C. et al. Intestinal inflammation targets cancer-inducing activity of the microbiota. *Science* **338**, 120–123 (2012).
28. Wu, L. N. et al. Sensitive and selective bacterial detection using tetracysteine-tagged phages in conjunction with biarsenical dye. *Angew. Chem. Int. Ed.* **50**, 5873–5877 (2011).
29. Rubinstein, M. R. et al. *Fusobacterium nucleatum* promotes colorectal carcinogenesis by modulating E-cadherin/β-catenin signaling via its FadA adhesin. *Cell Host Microbe* **14**, 195–206 (2013).
30. Sui, X. et al. Autophagy and chemotherapy resistance: a promising therapeutic target for cancer treatment. *Cell Death Dis.* **4**, e838 (2013).
31. Metch, J. W. et al. Metagenomic analysis of microbial communities yields insight into impacts of nanoparticle design. *Nat. Nanotechnol.* **13**, 253–259 (2018).
32. Liang, X. et al. Self-assembly of an amphiphilic Janus camptothecin-floxuridine conjugate into liposome-like nanocapsules for more efficacious combination chemotherapy in cancer. *Adv. Mater.* **29**, 1703135 (2017).
33. Pang, X. Y. et al. Inter-species transplantation of gut microbiota from human to pigs. *ISME J.* **1**, 156–162 (2007).
34. Stempler, O. et al. Interspecies nutrient extraction and toxin delivery between bacteria. *Nat. Commun.* **8**, 315 (2017).
35. Ritsma, L. et al. Surgical implantation of an abdominal imaging window for intravital microscopy. *Nat. Protoc.* **8**, 583–594 (2013).
36. Heijink, D. M. et al. Total abdominal ^{18}F-FDG uptake reflects intestinal adenoma burden in *Apc* mutant mice. *J. Nucl. Med.* **52**, 431–436 (2011).

Acknowledgements

Author contributions

D.-W.Z. and X.-Z.Z. conceived the project and designed the experiments. X.D. and D.-W.Z. synthesized materials. P.P and K.-W.C. performed in vitro microbiological experiments. X.D. performed in vitro cell experiments. D.-W.Z., X.D. and J.-X.F. collected and analysed the data. X.D., P.P. and K.-W.C. performed in vivo experiments. D.-W.Z., X.D., S.-X.C. and X.-Z.Z. co-wrote the manuscript. All of the authors discussed the results and reviewed the manuscript.

Competing interests

The authors declare no competing interests.

Additional information

Supplementary information is available for this paper at https://doi.org/10.1038/s41551-019-0423-2.

Reprints and permissions information is available at www.nature.com/reprints.

Correspondence and requests for materials should be addressed to X.-Z.Z.

Publisher's note: Springer Nature remains neutral with regard to jurisdictional claims in published maps and institutional affiliations.

nature research

Corresponding author(s):   Xian-Zheng Zhang

Last updated by author(s):   May 17, 2019

Reporting Summary

Nature Research wishes to improve the reproducibility of the work that we publish. This form provides structure for consistency and transparency in reporting. For further information on Nature Research policies, see Authors & Referees and the Editorial Policy Checklist.

Statistics

For all statistical analyses, confirm that the following items are present in the figure legend, table legend, main text, or Methods section.

n/a	Confirmed	
☐	☒	The exact sample size (*n*) for each experimental group/condition, given as a discrete number and unit of measurement
☐	☒	A statement on whether measurements were taken from distinct samples or whether the same sample was measured repeatedly
☐	☒	The statistical test(s) used AND whether they are one- or two-sided *Only common tests should be described solely by name; describe more complex techniques in the Methods section.*
☒	☐	A description of all covariates tested
☐	☒	A description of any assumptions or corrections, such as tests of normality and adjustment for multiple comparisons
☐	☒	A full description of the statistical parameters including central tendency (e.g. means) or other basic estimates (e.g. regression coefficient) AND variation (e.g. standard deviation) or associated estimates of uncertainty (e.g. confidence intervals)
☐	☒	For null hypothesis testing, the test statistic (e.g. *F*, *t*, *r*) with confidence intervals, effect sizes, degrees of freedom and *P* value noted *Give P values as exact values whenever suitable.*
☒	☐	For Bayesian analysis, information on the choice of priors and Markov chain Monte Carlo settings
☒	☐	For hierarchical and complex designs, identification of the appropriate level for tests and full reporting of outcomes
☒	☐	Estimates of effect sizes (e.g. Cohen's *d*, Pearson's *r*), indicating how they were calculated

Our web collection on statistics for biologists contains articles on many of the points above.

Software and code

Policy information about availability of computer code

Data collection	No software was used.
Data analysis	All statistical analyses were performed on Origin (version 8.6), SPSS (version 22), Graphpad Prism 7 or Excel 2016. Living Image software (Perkin Elmer) was used to analyze bioluminescent and fluorescent images. Image J (Version 1.48h3) was used for fluorescence-image analysis. Omics data were analyzed online with I-Sanger Cloud Platform.

For manuscripts utilizing custom algorithms or software that are central to the research but not yet described in published literature, software must be made available to editors/reviewers. We strongly encourage code deposition in a community repository (e.g. GitHub). See the Nature Research guidelines for submitting code & software for further information.

Data

Policy information about availability of data

All manuscripts must include a data availability statement. This statement should provide the following information, where applicable:

- Accession codes, unique identifiers, or web links for publicly available datasets
- A list of figures that have associated raw data
- A description of any restrictions on data availability

The authors declare that the main data supporting the results in this study are available within the paper and its Supplementary Information. The raw and analysed datasets generated during the study are available for research purposes from the corresponding authors on reasonable request.

Field-specific reporting

Please select the one below that is the best fit for your research. If you are not sure, read the appropriate sections before making your selection.

☒ Life sciences ☐ Behavioural & social sciences ☐ Ecological, evolutionary & environmental sciences

For a reference copy of the document with all sections, see nature.com/documents/nr-reporting-summary-flat.pdf

Life sciences study design

All studies must disclose on these points even when the disclosure is negative.

Sample size	Sample sizes were determined according to previous experimental experience.
Data exclusions	No data were excluded.
Replication	All experimental findings could be reliably reproduced.
Randomization	All samples/organisms were randomly allocated into experimental groups.
Blinding	Blinding and randomization were applied to all experiments.

Reporting for specific materials, systems and methods

We require information from authors about some types of materials, experimental systems and methods used in many studies. Here, indicate whether each material, system or method listed is relevant to your study. If you are not sure if a list item applies to your research, read the appropriate section before selecting a response.

Materials & experimental systems

n/a	Involved in the study
☐	☒ Antibodies
☐	☒ Eukaryotic cell lines
☒	☐ Palaeontology
☐	☒ Animals and other organisms
☐	☒ Human research participants
☒	☐ Clinical data

Methods

n/a	Involved in the study
☒	☐ ChIP-seq
☐	☒ Flow cytometry
☒	☐ MRI-based neuroimaging

Antibodies

Antibodies used	Anti-cleaved caspase3 (GB11009), anti-caspase9 (GB11053-1), anti-LC3A/B (GB11124) and anti-P62 (GB11531) rabbit polyclonal monoclonal antibodies from Servicebio. Anti-Ki67 monoclonal antibody [sp6] was purchased from Genetex.
Validation	Validations were conducted by the respective manufacturer as noted on the antibody specification sheet.

Eukaryotic cell lines

Policy information about cell lines

Cell line source(s)	CT26 colon cancer cells, HT29 colon cancer cells and HCT116 colon cancer cells were all obtained from China Center for Type Culture Collection (CCTCC).
Authentication	Each cell line used was morphologically confirmed according to the information provided by ATCC.
Mycoplasma contamination	All cell lines were tested for mycoplasma contamination. No mycoplasma contamination was found.
Commonly misidentified lines (See ICLAC register)	No commonly misidentified cell lines were used.

Animals and other organisms

Policy information about studies involving animals; ARRIVE guidelines recommended for reporting animal research

Laboratory animals	Six-week-old BALB/c female mice (18 ± 2g), eight-week male C57BL/6J-ApcMin/+ mice and five week female Bama minipigs were

Laboratory animals	used for the study. C57BL/6J-ApcMin/+ mice were obtained from Nanjing Biomedical Research Institute of Nanjing University. BALB/c mice were purchased from Changsheng Biotechnology. Bama minipigs were purchased from Zixing Biotechnology.
Wild animals	The study did not involve wild animals.
Field-collected samples	The study did not involve samples collected from the field.
Ethics oversight	Experimental protocols were approved by the Institutional Animal Care and Use Committee (IACUC) of the Animal Experiment Center of Wuhan University (Wuhan, China). All animal experimental procedures were performed in accordance with the Regulations for the Administration of Affairs Concerning Experimental Animals approved by the State Council of People's Republic of China.

Note that full information on the approval of the study protocol must also be provided in the manuscript.

Human research participants

Policy information about studies involving human research participants

Population characteristics	Faecal samples from 72 clinical CRC patients and 52 controls. Patient baseline characteristics are available in Supplementary Table 1 of ref. 26.
Recruitment	No participants were recruited for this study.
Ethics oversight	This study did not involve collecting patient samples. It only uses data from the the NCBI bioproject (https://www.ncbi.nlm.nih.gov/sra/?term=PRJEB10878). No specific approval was required.

Note that full information on the approval of the study protocol must also be provided in the manuscript.

Flow Cytometry

Plots

Confirm that:

☒ The axis labels state the marker and fluorochrome used (e.g. CD4-FITC).

☒ The axis scales are clearly visible. Include numbers along axes only for bottom left plot of group (a 'group' is an analysis of identical markers).

☒ All plots are contour plots with outliers or pseudocolor plots.

☒ A numerical value for number of cells or percentage (with statistics) is provided.

Methodology

Sample preparation	Cells were cultured on 6-well plates with a density of 1×10^5 cells per well and were constitutively transfected with mCherry-GFP-LC3. After being treated with PBS, IDNP (30 μM), IDNP (30 μM) + Fn (1×10^7 CFU) and phage + IDNP (30 μM IDNP + 1×10^7 CFU Fn + 1×10^8 PFU phage), respectively and co-incubated for 4 h, flow cytometry was used to analyze autophagy effect of Fn.
Instrument	BD Accuri™ C6 flow cytometer, model:Facscalibur, manufacturers :BD
Software	Data were analysed on Flowjo V10 (Treestar, 139 Ashland, USA).
Cell population abundance	Flow cytometry was used for quantification only. No post-sort fractions were collected.
Gating strategy	Cells were first gated on FSC/SSC. Singlet cells were usually gated using FSC-H and FSC-A. GFP and mCherry gating were performed on the live cell population.

☒ Tick this box to confirm that a figure exemplifying the gating strategy is provided in the Supplementary Information.